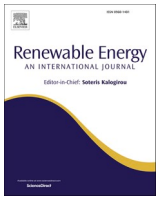
Renewable Energy 253 (2025) 123600



Contents lists available at ScienceDirect

Renewable Energy

journal homepage: www.elsevier.com/locate/renene



A numerical study on a solar chimney integrated with latent heat thermal energy storage in various arrangements

Sergio Nardini *, Bernardo Buonomo, Maria Rita Golia, Oronzio Manca

Dipartimento di Ingegneria, Università degli Studi della Campania "Luigi Vanvitelli", Via Roma 29, Aversa, CE, Italy

ARTICLE INFO

Keywords:
Solar chimney
Natural ventilation
Thermal energy storage
Energy efficiency in building

ABSTRACT

This paper presents a two-dimensional numerical analysis of a solar chimney integrated with an absorbent wall on the south façade of a building. The investigation was carried out in July and December in Aversa, Italy, from sunrise to dusk. The solar chimney features a converging channel, a vertical absorbing wall, and a glass plate slanted at two degrees. A thermal energy storage system comprising phase change material and metal foam behind the absorbing wall was evaluated. Using Ansys-Fluent, four configurations were analyzed to identify the optimal layout for thermal performance. Key findings include liquid fraction, energy storage, mass flow rate, velocity profiles, and wall temperature distributions. Additionally, the study assesses collector efficiency and energy density, offering insights for system optimization. When the box is placed along the entire vertical wall (Configuration D), it demonstrates the highest efficiency, achieving 57 % in July for a volume of 0.06 m^3. The box positioned at the bottom of the vertical wall (Configuration A) records the highest peak mass flow rates but exhibits less uniform behavior, similar to Configuration B, where the box is placed in the center of the vertical wall. Meanwhile, the box positioned at the top of the vertical wall (Configuration C) shows a 65 % increase in energy accumulation in July and 61 % in December when the volume is tripled.

Nomenclature

A	Area, m^2		
b_{max}	Width of the inlet section, m	*Greek symbol*	
b_{min}	Width of the outlet section, m	α	Absorbivity
c_p	Specific heat, J kg^{-1} K^{-1}	β	Liquid fraction
L	Height of the chimney, m	γ	Thermal expansion coefficient, K^{-1}
L_h	Height of the thermal energy storage, m	ϵ_e	Emissivity
h	Specific enthalpy, kJ kg^{-1}	ϵ_p	Porosity
g	Gravity acceleration, m s^{-2}	λ	Thermal conductivity, W $m^{-1}K^{-1}$
F	View factor	μ	Viscosity, kg $m^{-1}s^{-1}$
L	Height of the chimney, m	ρ	Density, kg m^{-3}
H	Enthalpy, J	ρ_E	Energy density, MJ m^{-3}
h_l	Latent heat of PCM, J kg^{-1}	σ	Stephan Boltzmann const, Wm^{-2} K^{-4}
s	Thickness, m	ω	Pore size, PPI
T_s	Solidus temperature, K	*Subscripts*	
T_l	Liquidus temperature, K	0	Operating
T_w	Wall temperature, K	mf	Metal foam
		pcm	Phase change material
		i	Initial
		P	Surface P

1. Introduction

The use of fossil fuels for heating and cooling of environments is a problem that is being addressed in recent years. One of the ways in which it could impact energy consumption less and achieve more comfortable conditions is to implement the solar chimney in buildings. The solar chimney is a passive solar heating and cooling system in which the buoyancy of warm air caused by the solar radiation is employed to speed up the airflow through the system [1–3]. Much research has been conducted on the solar chimney to demonstrate how the use of PCM increases its thermal performance, and it is pointed out how the characteristics of PCMs have a substantial impact on overall chimney performance.

To the best of our knowledge, PCM offers a lot of possibilities for improving building thermal comfort, extending ventilation time, and enhancing solar chimney power plant energy output [4].By utilizing phase change material (PCM), a Solar Chimney combined with Latent Heat Thermal Energy Storage System (LHTESS), can achieve high

* Corresponding author.
E-mail address: sergio.nardini@unicampania.it (S. Nardini).

https://doi.org/10.1016/j.renene.2025.123600
Received 10 November 2023; Received in revised form 21 May 2025; Accepted 29 May 2025
Available online 31 May 2025
0960-1481/© 2025 The Author(s). Published by Elsevier Ltd. This is an open access article under the CC BY license (http://creativecommons.org/licenses/by/4.0/).

thermal operating efficiency in both summer and winter. During the cold season, the system can warm the indoor environments because of the storage effect of PCMs; meanwhile, during the hot season, the indoor spaces are cool thanks to the solar chimney that pushes warm air outside [5,6].

One of the first investigations regarding solar chimneys with phase change material was conducted by Kotani et al. [7] proposed a breakthrough idea of the solar chimney with a sodium sulfate decahydrate as PCM with a melting point of 32 °C encapsulated in rectangular slab to create a latent heat storage system. They assessed a numerical simulation and validated it with experiments on prototype of solar chimney with built-in PCM module. They analyzed two cases, when the PCM did not melt and when PCM completely melted and observed that the simulation and experiment findings showed that the combination of PCM storage within the solar chimney is highly beneficial but also that, even if the PCM totally melted during the day, it can still provide a constant daily average airflow rate of 155 m^3/h during the evening and night. Lastly, the prototype solar chimney can produce an average airflow of over 200 m^3/h during the day. The paper of Sharma et al. [8] continued the work of Kotani and noted that integrating the PCM inside the solar chimney the system can generate a nearly constant average airflow of 155 m^3/h. Moreover, Kaneko et al. [9] measured the result of the flow rate in the prototype of the chimney and found that the prototype chimney supplies the airflow rate of 100–400 m^3/h that could include the flow rate prompted by the wind. Amori and Mohammed [10] prove how adding paraffin wax to the solar chimney increases the ventilation time after dusk and calculates the thermal efficiency. They conducted experimental evaluations and studied various air inlet sites. It was observed that the solar chimney with a lateral entry had the optimum thermal efficiency and when both the bottom and side gates are opened, the maximum air temperature at the chimneys' outflow is 52 °C, compared to 61 °C for the bottom entry. The PCM changed the thermal performance of the chimney and increased the ventilation hours during the absence of sunlight or at night discharging the stored energy. Fadei et al. [11] analyzed two configurations of solar chimney (SC), with PCM and without PCM. They pointed out that the thermal performance of SC is improved adding latent heat thermal storage system. The results show that the maximum absorber surface temperature is 4° difference from the SC-PCM (72 °C) and the conventional SC (69 °C). Also, the maximum air velocity is a bit higher in SC-PCM, 2 m/s compared to 1.9 m/s of classical SC. It indicates that employing the LHS increases average mass flow rate by around 8.33 %, which boosts SC efficiency.

More and more methods are being used to improve the efficiency of the solar chimney. Long et al. [12] analyzed the pros of a solar chimney with phase change material integrated with an earth-air heat exchanger (SCEAHE) by using a validated mathematical model, during summertime. The integration of PCM increased the SCEAHE system's thermal inertia. According to the findings the absorber surface temperature with PCM was 78.8 °C, 16.2 % lower than it would have been without PCM. For the SCEAHE with and without PCM, the greatest temperature differential between the input air and exit air was around 13.3 °C and 12.7 °C. Using the SCEAHE with PCM, the maximum interior air temperature was lowered by 0.8 °C. The thermal comfort and the cooling capacity is increased in a SCEAHE system with PCM. Cao et al. [13] they proposed and investigated a novel solar chimney ventilator (SCV) using phase change material combined with photovoltaic (PV) technology (SCV-PV-PCM). They emphasized that air circulation is a crucial component of human productivity and well-being in both residential and commercial constructions. The system was examined in realistic Hong Kong weather in daylight hours throughout various seasons of the year. It was noted that the SCV-PV-PCM generated more power and ventilation capacity than those of the standard SCV-PV system. In particular, the electrical performance is 14.8 % and the and the ventilation capacity is 7.6 % higher than the SCV-PV system. Lastly, ASHRAE was used to assess the air quality that the PCM system produced. Nateghi and Jahangir [14] analyzed the thermal comfort that a solar chimney with phase change material can provide in a building in different climate zone: hot-arid climate, hot-humid and cold semi-arid. They analyzed the comfort in term of PVM thermal index, which is ideal between −0.7 and + 0.7. They noted that in hot-arid climate the presence of solar chimney with a layer of PCM causes discomfort and highlight how the benefit of solar chimney strongly depends on weather conditions. Tariq et al. [15] highlighted how integrating energy storage in buildings can be difficult and how digital, global-scale resources based on methodological approaches validated by data obtained through simulations and experiments are needed to find the best solutions. In this paper they aim to explain and create a digital twin that can return valid results. They analyzed the building for 4 different climate area, taking in account the climate boundary of each area and varying the parameters that affect the performance of solar chimney to obtain best results.

Numerical simulations of Liu and Li [16] demonstrate that system performance rapidly declines below a heat flow of 500 W/m^2, and that there is little to no increase at a heat flux of 700 W/m^2. The experimental investigations in Ref. [17] analyzed three distinct charging modes: closed-fully charging mode, open-partly charging mode, and open-fully charging mode and show that the melting time of PCM in the open-fully charging state was over 11 h, which was 57 % longer than it was in the closed mode. During the phase shift period, the average airflow rate was 0.04 kg/s. Li et al. [18] illustrated that melting requires longer time to complete than freezing at higher phase change temperature. This demonstrates that while the PCM with lower phase change temperature is more charged than the other PCMs, it releases the latent heat it has accumulated more slowly. This shows that decreasing the phase transition temperature by 10 °C shortens the solidification time by almost 70 % and shortens the melting time by almost 50 %. Tiji et al. [19] compared the simulation of a PCM-enhanced solar chimney with system without PCM. They studied temperature and velocity distributions inside a guardhouse and concluded that, compared to a system without fins, finned storage can significantly recover energy losses while simultaneously increasing the average room temperature by 20 %. The inclusion of the fins increases the flow velocity by about 40 % and contributes to the non-uniformity of airflow in the room. Xamàn et al. [20] analyzed numerical simulation of three different configuration with copper plate, PCM (46–50) and concrete wall orientated to the east, south and west to analyze the overall thermal performance. They noted that Solar chimney with a concrete wall exhibiting the lowest efficiency and the average thermal efficiencies of the solar chimney with PCM is 27 % and with copper plate is 34 % for south orientation. Moreover, they observe that PCM layer remains in the mushy zone for the east and south orientation.

Metal foam is an excellent method to enhance thermal energy storage with phase change material. The advantages of PCM embedded in metal foam have been examined [21]. Ashouri and Hakkaki-Fard [22] investigated an inclined rooftop solar chimney with a photovoltaic panel combined with fins absorber and PCM. They developed a 3D model where the governing equations were solved by means of the Finite Volume Method. They investigated the effect of the fin thickness and number as well as the effect of different mass of PCM and how to change the ventilation rate of the system with different pure PCM and composite PCM. They noted that combined copper foam and PCM in the SC-PCM-PV system the ventilation duration is extend due to the high conductivity of copper foam.

Zhu et al. [23] in their paper analyzed the thermal performance of a solar chimney with and without phase change material (PCM) at different inclination angles (30°, 45°, and 60°). The results showed that the inclination angle significantly affects convective heat transfer within the PCM. The optimal angle was found to be 45°, where the maximum air velocity was achieved (0.37 m/s with PCM and 0.4 m/s without PCM). Additionally, the system with PCM provided extended ventilation for over 10 h after the heat source was removed, even with reduced heat fluxes (200 W/m^2).

Buonomo et al. [24] studied one hybrid solar chimney enhanced

with a latent heat thermal energy storage with PCM and metal foam where the thermal energy storage is equal to the length of the channel height. The analyses are conducted only on June 21 in the transient regime and the findings indicated that the PCM did not entirely melt, but its temperature rises independent of radiant energy. Additionally, the PCM lowers the wall temperature, and it allows to absorb more energy during the hotter hours and release it during the colder hours. In another investigation Buonomo et al. [25] analyzed and compared the results of three different thickness of the thermal storage system (1.5 cm, 2.5 cm and 5.0 cm) in transient regime on 21 of June. They noted that the PCM-MF thermal energy storage reduced the variation of the temperature along the day and in the case with only-PCM thermal energy storage the completely melt is not reached.

This short review underscores the scarcity of investigations on solar chimneys with composite phase change materials (PCMs) and (PCMs with metal foam) in the current open literature and aims to cover the several features related to the phenomenological aspects that have not been sufficiently investigated. The focus of this work is to explore the aspects related to the transient regime resulting from the daily variations in solar radiation and changes in climatic data. Furthermore, it is worth highlighting the limited availability of articles addressing the application of solar chimneys for domestic use. Specifically, starting from the geometry and results of Buonomo et al. [24–26] the aim was to analyze the different configurations in more detail the phenomenological thermal and fluid-dynamic behavior. In fact, the previous works [24,25] were preliminary investigations and [26] did not take into consideration some thermal and fluid dynamics parameters, such as the stream function with liquid fraction, and the parameters related to the efficiency of system were not analyzed. Behind the absorbing vertical wall is placed a box with paraffin wax embedded in aluminum metal foam with given porosity values and pores per inch (PPI). Eight alternative configurations were investigated: six configurations are related to the box with the height equal to half of the length of the vertical wall and located at top, middle or bottom of the wall with two different thickness. The other two configurations are related to the box with the same height of the vertical wall located all along the wall, also in this case, with two different thickness. The governing equations for the transient analysis are the k-ε turbulence model and a two-dimensional airflow model, and they are resolved with the application of Ansys-Fluent commercial code. The research is conducted in the months of July and December, at Aversa (Italy) from dawn to dusk. Liquid fractions, stored energy, stream function fields, as well as channel wall temperature distributions, are used to express the results. The efficiency of the solar chimney was also assessed by incorporating the thermal energy storage unit, and the energy density for the different cases under examination was computed. It is worth underlining that in the present work a direct link between local and global thermal, and fluid dynamic behaviors and the efficiency parameters is given, for the first time, for a solar chimney with a latent thermal energy storage composed by PCM and metal foam.

2. Mathematical model

Fig. 1a shows the solar chimney integrated into a building and Fig. 1b shows the solar chimney in 3D. The dimensions chosen and reported in Table 1 refer to what could be a typical solar chimney in a single-family house. These dimensions do not prevent the physical model from being scalable to larger sizes.

Fig. 2 shows the configuration of solar chimney, while Table 1 lists its geometrical specifications. It consists of a channel with the absorbing vertical wall with a height equal to L = 4.00m. The glass of the chimney is a low-emissivity glass wall that is tilted at an angle of 2° to the vertical. The inclination angle was chosen taking into account the results presented in Refs. [2,3] where the optimal thermal conditions were realized. The phase change material is encased in aluminum foam and placed within a rectangular box with a height of "L/2″ and a thickness of "s," where *s* is equal to 0.03 m or 0.01 m in configurations A, B, and C,

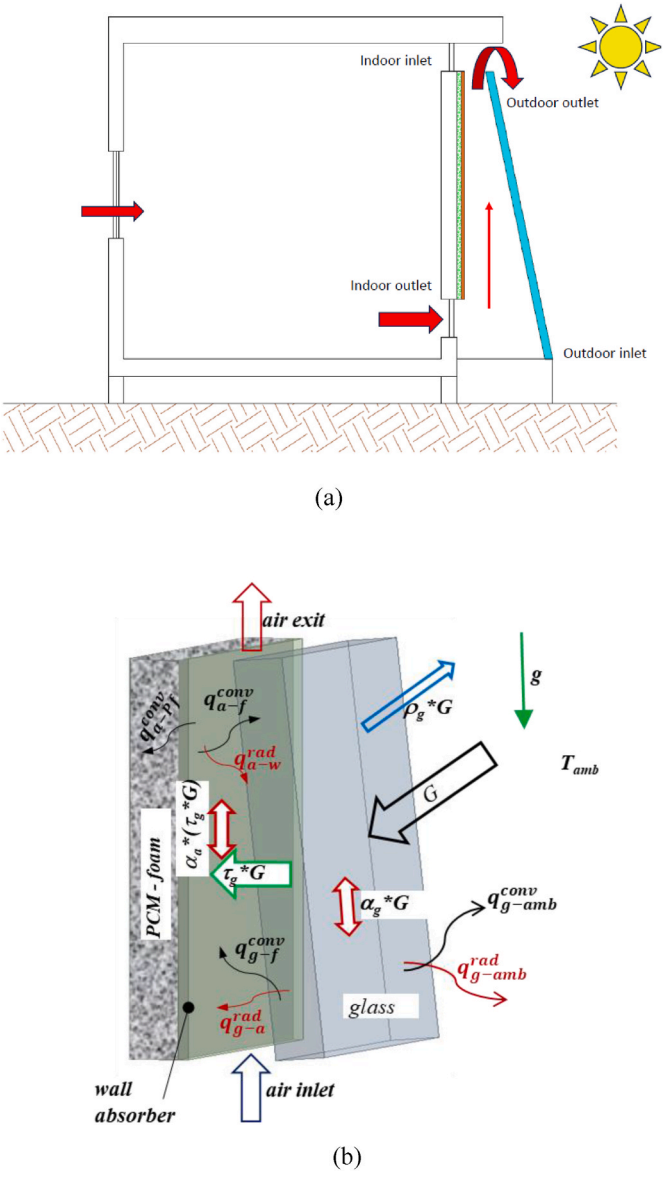


Fig. 1. (a) Representation of the solar chimney in a building and (b) 3D representation.

Table 1
Solar chimney and TES dimensions referring to Fig. 1.

Case	Hight TES, L [m]	Thickness, s [m]	b_{max} [m]	b_{min} [m]
A, B and C	2.00	0.03 0.01	0.34	0.20
D	4.00	0.015 0.005	0.34	0.20

and equal to 0.015 m and 0.005 m in configuration D, in order to maintain the same volume of PCM. The inlet and the exit sections of the channel, respectively, are denoted by b_{max} = 0.34m and b_{min} = 0.20m.

The selected configurations, at different heights of the vertical wall, were designed to observe how the wall temperature changes throughout the day and how the chimney ventilation varies depending on the position of the PCM box, as well as to assess how the thickness of this box can affect these data. In solar chimney designs, the section at the top is often narrower to enhance the chimney's efficiency in promoting airflow. This narrowing increases the velocity of the rising warm air, which helps improve the natural ventilation process. The choice of PCM,

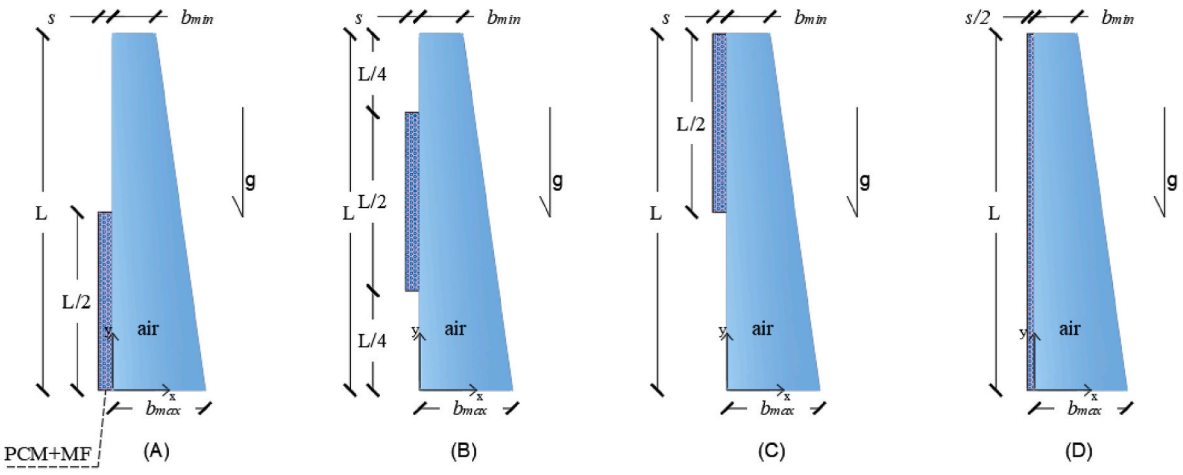


Fig. 2. Solar chimney sketch.

paraffin wax 42, was not random; it was made following an analysis of three paraffins with different melting points: paraffin wax 31, 42, and 57. This decision was based on their behavior in relation to the typical ambient temperature of the chosen location. It was found that paraffin 42 exhibited the best characteristics in terms of melting and solidification speed, as well as maintaining ventilation even after sunset.

It is assumed that the compression work and viscous dissipation are negligible. A two-dimensional (2D), incompressible, turbulent, and transient flow has been considered for the air passing through the chimney. Furthermore, the properties of air and PCM are assumed to be independent of temperature. Following is reported the governing equations for air-zone (mass, momentum, and energy), known as Reynolds-Averaged Navier-Stokes (RANS).

$$\frac{\partial u_i}{\partial x_i} = 0 \tag{1}$$

$$\rho \cdot \left(\frac{\partial u_i}{\partial t} + u_j \cdot \frac{\partial u_i}{\partial x_j}\right) = -\frac{\partial P}{\partial x_i} + \frac{\partial}{\partial x_j}\left[\mu \cdot \left(\frac{\partial u_i}{\partial x_j} + \frac{\partial u_j}{\partial x_i}\right) - \rho \cdot \overline{u_i' u_j'}\right] + \rho \cdot g_i \cdot \gamma \cdot (T - T_0) \tag{2}$$

$$\rho \cdot C_p \cdot \left(\frac{\partial T}{\partial t} + u_i \cdot \frac{\partial T}{\partial x_i}\right) = \frac{\partial}{\partial x_i} \cdot \left[\lambda \cdot \frac{\partial T}{\partial x_i} - \rho \cdot C_p \cdot \overline{u_i' T}\right] + S_{rad} \tag{3}$$

where x_i is the coordinate along x-direction for $i = 1$ and y-direction for $i = 2$, respectively. The variables: u_i, T and P represent the velocity components in the x_i-directions, the temperature, and the pressure of the air, respectively.

The Boussinesq model is used to describe the turbulent Reynolds stresses in momentum Eq. (2) ($\rho\overline{u_i' u_j'}$) and the turbulent heat transfer in energy Eq. (3) ($\rho\overline{u_i' T}$) [27,28].

$$\rho\overline{u_i' u_j'} = \mu_t\left(\frac{\partial u_i}{\partial x_j} + \frac{\partial u_j}{\partial x_i}\right) - \frac{2}{3}\rho k \delta_{ij} \tag{4}$$

$$\rho\overline{u_i' T} = -\frac{\mu_t}{\mathrm{Pr}_t}\left(\frac{\partial T}{\partial x_j}\right) \tag{5}$$

Where μ_t is the turbulent eddy viscosity, d_{ij} is the Kronecker delta and Pr is the turbulent Prandtl number.

The S2S radiation model is denoted by S_{rad} and serves as the source term in the energy equation. Both the emitted and reflected energy fluxes are included in the radiant heat flux that leaves a surface. The expression for the energy flux departing from a given surface P is as follows [29]:

$$q_{out,P} = \varepsilon_{e,p}\sigma T_P^4 + (1 - \alpha)_p q_{in,P} \tag{6}$$

In Eq. (6), q_{out} represents the heat flux leaving the surface and q_{in} represents the heat flux incident on that surface. The emissivity of the surface P is $\varepsilon_e = 0.84$, the absorptivity is denoted by α and σ stands for the Stephan Boltzmann constant, equals to 5,67x 10^{-8} $\frac{W}{m^2K^4}$.

$$A_P q_{out,P} = \sum_{j=1}^{N} A_j q_{out}, F_{j,P} \tag{7}$$

The view factor $F_{j,P}$ between two surfaces determines the incident and exiting solar flux rates. Fj.k denotes the view factor of surface j with respect to surface P. In Eq. (7) A_P and A_j represent the areas of the surface P and j respectively.

Considering the reciprocity relation $F_{P,j} = F_{j,P}$, Eq. (6) can be expressed as:

$$Q_{out,P} = \varepsilon_{e,p}\sigma T_P^4 + (1 - \alpha)_p \sum_{j=1}^{N} Q_{out,j} F_{P,j} \tag{8}$$

The following is another way to explain Eq. (8) in terms of radiosity of the surface P:

$$J_P = E_P + (1 - \alpha_P) \sum_{j=1}^{N} F_{P,j} J_j \tag{9}$$

where emissive power of surface P is represented by E_P.

The k-ε model which was first proposed by Launder and Spalding [30] and then by Ayadi et al. [31], is considered to evaluate the turbulent viscosity.

The transport equations for the turbulent kinetic energy k and for the time rate dissipation ε are defined as:

$$\rho_{nf} u_j \frac{\partial k}{\partial x_j} = \frac{\partial}{\partial x_j}\left[\left(\mu_{nf} + \frac{\mu_t}{\sigma_k}\right)\frac{\partial k}{\partial x_i}\right] + G_k - \rho_{nf}\varepsilon \tag{10}$$

$$\rho_{nf} u_j \frac{\partial \varepsilon}{\partial x_j} = \frac{\partial}{\partial x_j}\left[\left(\mu_{nf} + \frac{\mu_t}{\sigma_\varepsilon}\right)\frac{\partial \varepsilon}{\partial x_i}\right] + C_{1\varepsilon}\frac{\varepsilon}{k}G_k - \rho_{nf} C_{2\varepsilon}\frac{\varepsilon^2}{k} \tag{11}$$

where the buoyancy and compressible effects are neglected, according to the hypotheses mentioned above. Moreover, G_k is the production of turbulent kinetic energy due to mean velocity gradients, which is given by:

$$G_k = -\rho_{nf}\overline{u_i' u_j'}\frac{\partial u_j}{\partial x_i} \tag{12}$$

and σ_k, σ_ε, $C_{1\varepsilon}$, $C_{2\varepsilon}$ are empirical constants, which are assumed as:

$$\sigma_k = 1.0, \sigma_\varepsilon = 1.3, C_\mu = 0.09, C_{1\varepsilon} = 1.44, C_{2\varepsilon} = 1.92 \quad (13)$$

μ_t is defined as:

$$\mu_t = \rho_{nf} C_\mu \left(\frac{k^2}{\varepsilon}\right) \quad (14)$$

where C_μ is empirical constant, $\left(\varepsilon = \left(\mu_{nf}/\rho_{nf}\right)\overline{(\partial u_i'/\partial x_j)(\partial u_i'/\partial x_j)}\right)$ is the turbulence dissipation rate.

In this work, it is assumed that the heat transfer between PCM and metal foam is described by the local thermal equilibrium (LTE). For completeness, the governing equations of the PCM are included. However, since the PCM box has a negligible thickness compared to the structure of the chimney, the convective part of the PCM has been omitted, and the analysis has been conducted using conductive melting. In the equations, the natural convection of liquid phase is simulated using the Boussinesq approximation, while the metal foam is represented as an isotropic, homogenous porous medium. The governing equations are the following and they are two-dimensional, unsteady, and laminar:

$$\frac{\partial u_i}{\partial x_i} = 0 \quad (15)$$

$$\frac{\rho_{pcm}}{\varepsilon_p}\cdot\left(\frac{\partial u_i}{\partial t} + \frac{u_j}{\varepsilon_p}\cdot\frac{\partial u_i}{\partial x_j}\right) = -\frac{\partial p}{\partial x_i} + \frac{\mu_{pcm}}{\varepsilon_p}\cdot\frac{\partial^2 u_i}{\partial x_j^2} + S_{xi} \quad (16)$$

$$(\rho c)_{eff}\cdot\left(\frac{\partial T}{\partial t}\right) = k_{eff}\cdot\left(\frac{\partial^2 T}{\partial x_i^2}\right) - \varepsilon_p\cdot\rho_p\cdot H_L\cdot\frac{\partial \beta}{\partial t} \quad (17)$$

Under the Boussinesq approximation ρ_p is the density of the PCM that depends on temperature, μ_{pcm} is the viscosity of the liquid PCM and p is the pressure.

In Eq. (17) H_L represents the latent heat of the PCM, and t is the time.

The weighted average value for the specific heat and the effective thermal conductivity are reported in Eqs. (18) and (19), respectively [32]:

$$(\rho c)_{eff} = (1-\varepsilon_p)\rho_{mf} c_{mf} + \varepsilon_p \rho_{pcm} c_{pcm} \quad (18)$$

$$k_{eff} = A\left[\varepsilon_p k_{pcm} + (1-\varepsilon_p)k_{mf}\right] + \frac{1-A}{\left[\frac{\varepsilon_p}{k_p} + \frac{(1-\varepsilon_p)}{k_{mf}}\right]} \quad (19)$$

where ρ_{mf}, ρ_{pcm} and c_{mf}, c_{pcm} represent the density and specific heat of metal foam (mf) and PCM (p), while ε_p is the porosity of metal foam. k_{mf} and k_{pcm} are the metal foam and PCM thermal conductivities. In eq. (19) A is equal to 0.35 as proposed by Bhattacharya et al. [32].

The vector S_{xi} is the source term described in Ref. [33]:

$$S_{xi} = -\frac{(1-\beta)^2}{\left(\beta^3 - 0.001\right)^3}\cdot A_{mush}\cdot u_i - \frac{\mu_{pcm}}{K}\cdot u_i - \frac{C_F}{\sqrt{K}}\cdot\rho_{pcm}\cdot u_i\cdot\sqrt{u_i^2 + u_j^2} + \rho_{pcm}\cdot g_i\cdot\gamma\cdot(T - T_m) \quad (20)$$

To simulate the solidification and melting of the PCM, Voller and Prakash's [34] enthalpy-porosity approach is employed and using that approach, it can consider that there is a mixed solid-liquid zone during the melting process instead of a perceivable separation between the solid and liquid zones. The porosity of material decreases from 1 to 0 when it solidifies. The porosity is between 1 and 0 is referred to as a pseudo-porous media zone. The mixed region (also called as mushy zone) is described by a liquid fraction parameter β, whose values, when the region is entirely solid or liquid, range from 0 to 1, respectively.

The enthalpy-porosity approach is related to the first term in eq. (20), which mimics the existence of the solid component in the mixed zone. The amount 0.001 is assigned to prevent zero from going into the denominator when the liquid fraction goes to zero. A_{mush}, which stands for the velocity damping to zero during the solidification process and it is the constant in the mushy zone. According to Buonomo et al. [21], the constant A_{mush} has no effect on the melting's behavior when there is a metal foam in the system. In all numerical simulations the A_{mush} is set equal to 10^5 kg/m^{3}s, T_m is the melting temperature of PCM, g is the thermal expansion coefficient, provides for the buoyancy effect. Lastly, C_F represents the inertial drag factor and K denoted the permeability of metal foam.

The value of β is provided in eq. (21) and depends on the local temperature, T.

$$\begin{cases} \beta = 0 & \text{for} \quad T < T_s \\ \beta = \dfrac{T - T_s}{T_l - T_s} & \text{for} \quad T_s < T < T_l \\ \beta = 1 & \text{for} \quad T > T_l \end{cases} \quad (21)$$

When $T < T_s$ the domain is totally solid, and it is totally liquid when $T > T_l$. When $T_s < T < T_l$, occurs melting. In Table 2 are listed the parameters and properties of Paraffin wax 41–43 [20], and the aluminum foam with a porosity $\varepsilon_p = 0.955$ and 20 PPI [35] that were chosen as the PCM and metal foam for this investigation. It is assumed that the inlet section is at ambient pressure and temperature equal to 298.5 K in July and 285.29 K in December, which corresponds to the average daytime temperature. The heat flux, represented by solar radiation, is uniformly distributed over the absorbing plate and varies over time. The simulations started with velocity of the air equals to V = 0 m/s and $T = T_i$. Moreover, the unheated surfaces are considered adiabatic.

3. Numerical model

The numerical problem was solved by means Ansys Fluent (2020 R1) [36]. The Semi-Implicit Method for Pressure-Linked Equations (SIMPLE) was used to relate pressure and velocity. Energy and momentum equations and convective components were discretized using the second-order upwind method. The Surface-to-Surface (S2S) model was selected as the radiation model and the grey-diffuse model has been used with Ansys Fluent for the open channel with air within.

The average daily solar radiation in July and December is shown in Fig. 3.

The sensitivity of the mesh is evaluated by looking at four computational domains, Table 3, since the choice of mesh is a compromise between the quality of the solution and the computing time. For the sake of completeness, grid analyses are shown in Figs. 4 and 5.

The reference value "h" and the unidentified error value "h_x" are used to calculate the percentage error "$e_{h\%}$". In Fig. 4, the air velocity in the channel along the x-direction and the air temperature in the chimney for different computational grids are shown at a height of y = 2.00 m, for the case of December with a PCM box of thickness s = 1.00 cm at 12:45 p.m. It can be observed that the trends of the curves related to grid n.3 (61x196) and n.4 (81x256) are nearly overlapping and differ slightly. Specifically, the velocity peaks are slightly higher in grid n.4 compared to grid n.3, and the maximum difference in velocity values is observed between the sparsest mesh, 21x64, and the finest mesh, 81x256, at X = 0.10 m. However, the temperature trend is almost the same in the two

Table 2
Properties of the paraffin wax and aluminum foam [20].

Properties	Paraffin wax 41-43	Aluminum foam
Cp (J kg^{-1} K^{-1})	2100	2719
ρ (kg m^{-3})	829	871
λ (W m^{-1} K^{-1})	0.21	202.4
μ (kg m^{-1} s^{-1})	0.0055	–
γ (K^{-1})	0.004	–
H_L (kJ/kg)	228	–
T_s (K)	314.15	–
T_l (K)	316.15	–

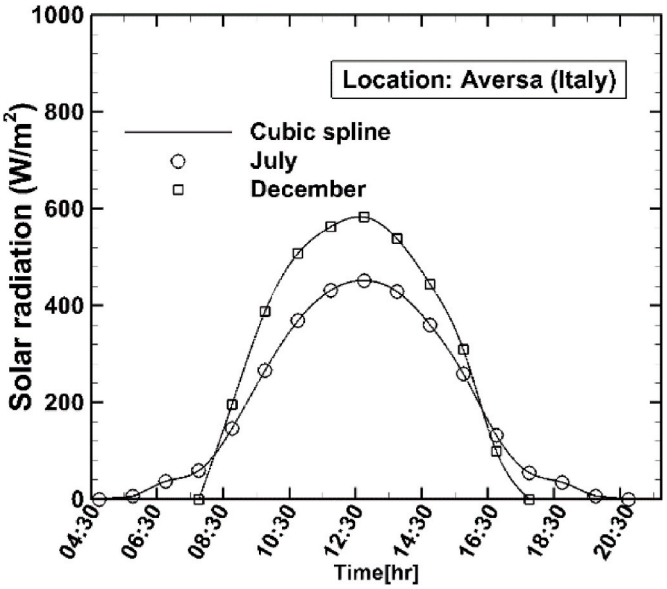


Fig. 3. Average daily solar radiation in July and December in the city of Aversa, Italy. PVGIS data (Symbol) and interpolating curves.

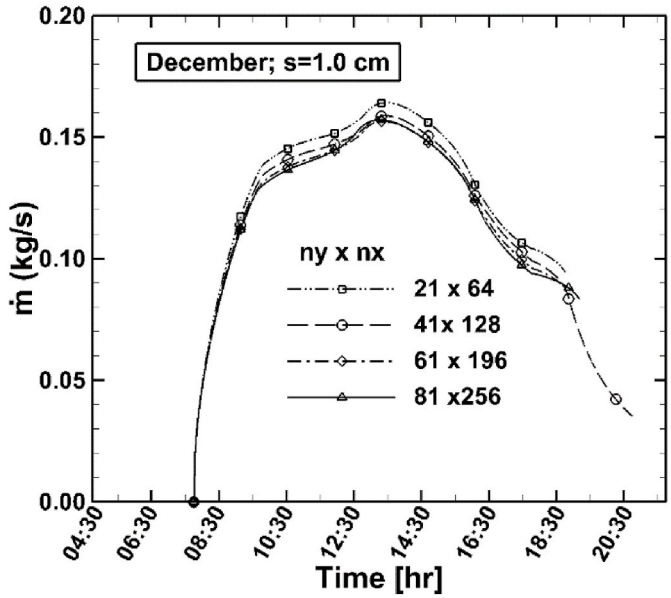


Fig. 5. Grid analysis (Average).

Table 3
Computational domains.

Mesh	1	2	3	4
Nx x Ny	21 x 64	41 x128	61 x 196	81 x 256
Total number of cells	1.344	5.248	11.956	20.736

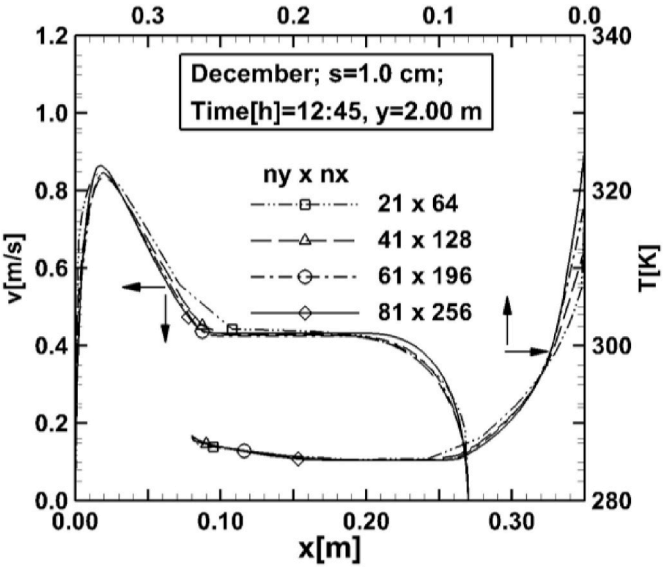


Fig. 4. Grid anlysis -local.

grids except for the final section, where grid n.4 reaches a slightly higher temperature than the simulation with grid n.3. The maximum discrepancy is observed near the wall. These differences decrease as the number of nodes in the mesh increases, and for grids n.3 and n.4, where the velocity and temperature profiles are practically overlapping, with the maximum percentage error values in Table 4. Fig. 5 illustrates the mass flow rate, also for the December case with s = 1.00 cm. Once again, grids n.3 and n.4 are almost overlapping. However, the maximum difference between the mass flow rate of the sparsest grid (n.1) and the densest grid (n.4) occurs at the peak temperature of the day at Time[h] = 13:45, with

Table 4
Grid analysis-local.

Mesh	Velocity error	Temperature error
1	11.5 %	15.0 %
2	3.99 %	8.0 %
3	2.1 %	1.14 %

Table 5
Grid analysis-Average.

Mesh	Flow rate error
1	6.3 %
2	3.0 %
3	0.8 %

the maximum percentage error values in Table 5.

After doing a sensitivity analysis, the grid mesh n.3 is selected because it offers the best performance for simulations while requiring the least amount of computational power.

$$e_{h\%} = \frac{|h_x - h|}{h}$$

To validate the model, a comparison was carried out with data in the paper by Gau and Viskanta [37], Fig. 6, where the fusion front at $\beta = 0.5$ for T = 311 K and H/W = 0.714 of the PCM is analyzed at 2, 6, 10, and 17 min to validate the phase change in the porous medium. It is observed that the experimental data are in good agreement with our model. Finally, in Fig. 7, the k-ε turbulence model for turbulent airflow in the channel is validated, and the data from the present numerical work are compared with the data from the experimental work of Myamoto et al. [38]. It is observed that the data provided in terms of dimensionless velocity profile are nearly overlapping with the experimental data.

For the D configuration on a selected day in July, a temporal independence analysis was conducted. To assess the accuracy of the temporal numerical solution, various time-step intervals (1, 5, 10, and 20 s) were tested on grid mesh no. 3. The analysis determined that a 10 s time-step was optimal for progressing in time, yielding a maximum deviation of around 0.20 % in the liquid fraction. The results obtained in the validation show a very good accordance with the literature data. In fact, the model used is similar to the behaviour observed in simulations and

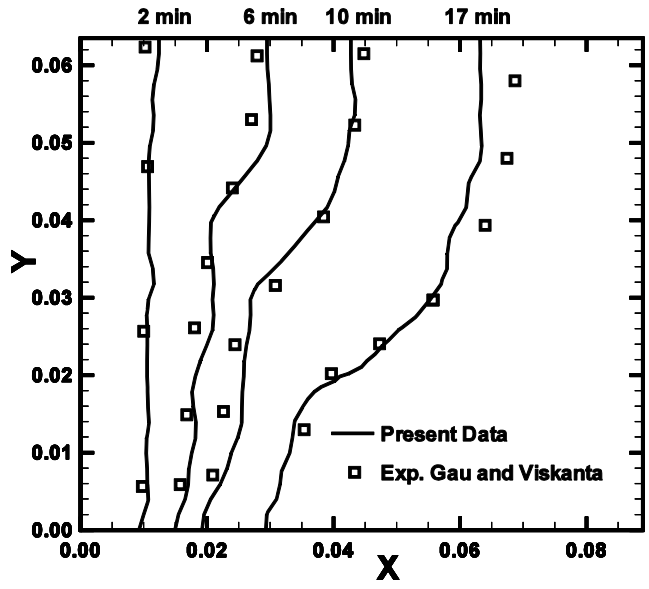


Fig. 6. Comparation between present data and experimental results by Gau and Viskanta [37]. Results in terms temporal evolution of the melt front location (β = 0.5) for T_h = 311K and H/W = 0.714.

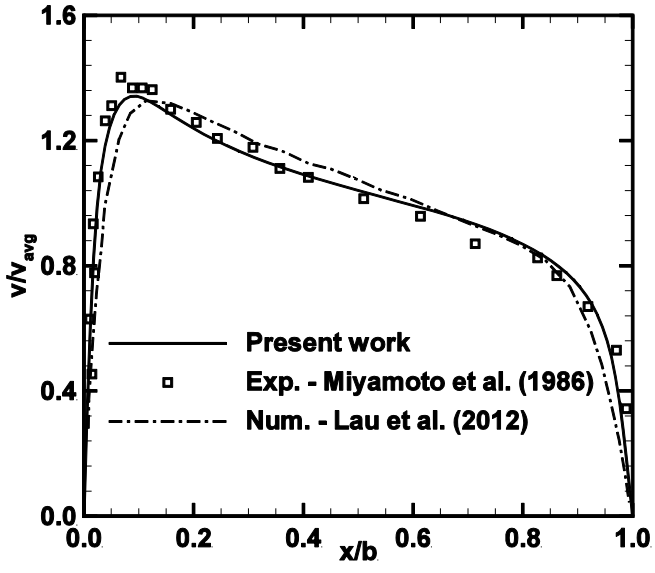


Fig. 7. Comparation between present data and experimental results by Miyamoto et al. [38] Results in terms dimensionless velocity profile q_w = 208 W/m^2, b = 0.1 m.

experiments conducted on the solar chimney. Therefore, the present model can be considered validated and reliable, as it replicates the behaviour of the solar chimney.

4. Results

The results of the thermal energy storage system integrated into the solar chimney are presented for the design days, July 21st and December 21st, covering the period from sunrise to a few hours after sunset. The results are presented in terms of local quantities, including velocity along the x-direction in the chimney channel, stream function fields, and wall temperature profiles, as well as global quantities such as the liquid fraction of the PCM, accumulated energy, mass flow rate, and parameters related to efficiency and energy density. All analyses were conducted for a typical day in both the summer and winter seasons in the city of Aversa, Italy.

The analysis of efficiency and energy density provides essential insights into the performance of system. Efficiency assessment quantifies how effectively the integrated system converts and utilizes thermal energy, aiding in evaluating its sustainability and operational feasibility. Meanwhile, examining energy density offers a deeper understanding of the energy storage capacity of system, underscoring its potential for consistent and reliable energy supply. Together, these analyses form a foundation for evaluating the overall operational effectiveness and long-term sustainability of the integrated solar chimney system with thermal energy storage.

4.1. Wall temperature

Fig. 8 shows a comparison of the wall temperature of the solar chimney with PCM and without PCM, acting as thermal energy storage. Time intervals at 12:45 (PCM charging phase) and 17:45 (discharging phase) were considered for both July and December, for Configuration B (Fig. 8a-c) and Configuration D (Fig. 8b-d). It is noted that for low thicknesses of s = 1.00 cm and s = 0.50 cm, the wall temperature is scarcely influenced by the presence of Thermal Energy Storage. However, for higher thicknesses of s = 3.0 cm and s = 1.50 cm, the wall temperature shows less variation throughout the day. Furthermore, by comparing Fig. 8a and c and Fig. 8b and d, the aim is to highlight the different behaviors during the loading and unloading phase of the TES. In fact, if during the loading phase (12:45) the wall in contact with the TES had a lower temperature compared to the wall without TES, during the unloading phase (17:45) when the sun is about to set or has set, the wall in contact with the TES has a higher temperature than the wall of the chimney without TES. Fig. 8 also demonstrates the difference in behavior based on the variation of the thickness of the TES with PCM, which is more evident when the thickness of the PCM is greater. Therefore, greater attention will be given to TES with thicknesses of s = 3.0 cm and s = 1.50 cm.

The evolution of the wall temperature profile is reported for the A, B and C configurations, Fig. 9, and for the configuration D, Fig. 10, with a thickness of PCM-MF storage equal to s = 3.0 cm, in July and December. As seen in Fig. 9a, 9.c and 9.e, during the month of July, configurations A, B and C show an almost constant temperature in the adjacent area with the PCM + MF, and great temperature differences depending on the time of day in the area of the wall without the PCM + MF, which heats up a lot at 12:45 p.m. and cools down sharply at 6:45 p.m. During December, Fig. 9b, 9.d and 9.f, it is observed that the temperature of the wall adjacent to the box of PCM + MF rises and after 9:45 a.m. becomes almost constant. Fig. 10 shows the trends of the wall temperature when it is all adjacent to the box of PCM and Metal foam. In Fig. 10a, which represents the wall temperature during July, the temperature is more homogeneous and constant, and at 3:45 p.m. this is the only configuration where the wall with PCM + MF exceeds 320K. The temperature profiles are almost overlapping. In Fig. 10b, showing the month of December, a similar behavior can be observed but with temperature profiles further apart, particularly at 9:45 a.m. the temperature starts to rise and then becomes almost constant from 12:45 p.m. onwards. The presence of the PCM + MF causes the wall temperature to remain nearly constant, and the temperature differences during the day is significantly lower than in the rest of the wall. A more constant and higher temperature during the day makes it possible to prolong the operation of the solar chimney even after sunset. It is worth noticing that the box of PCM + MF in configuration D was made to be equal in volume to configurations A, B and C, and this affected the thickness of the layer.

4.2. Average temperature of phase change material

In Fig. 11 is shown the average temperature trend of the PCM, during

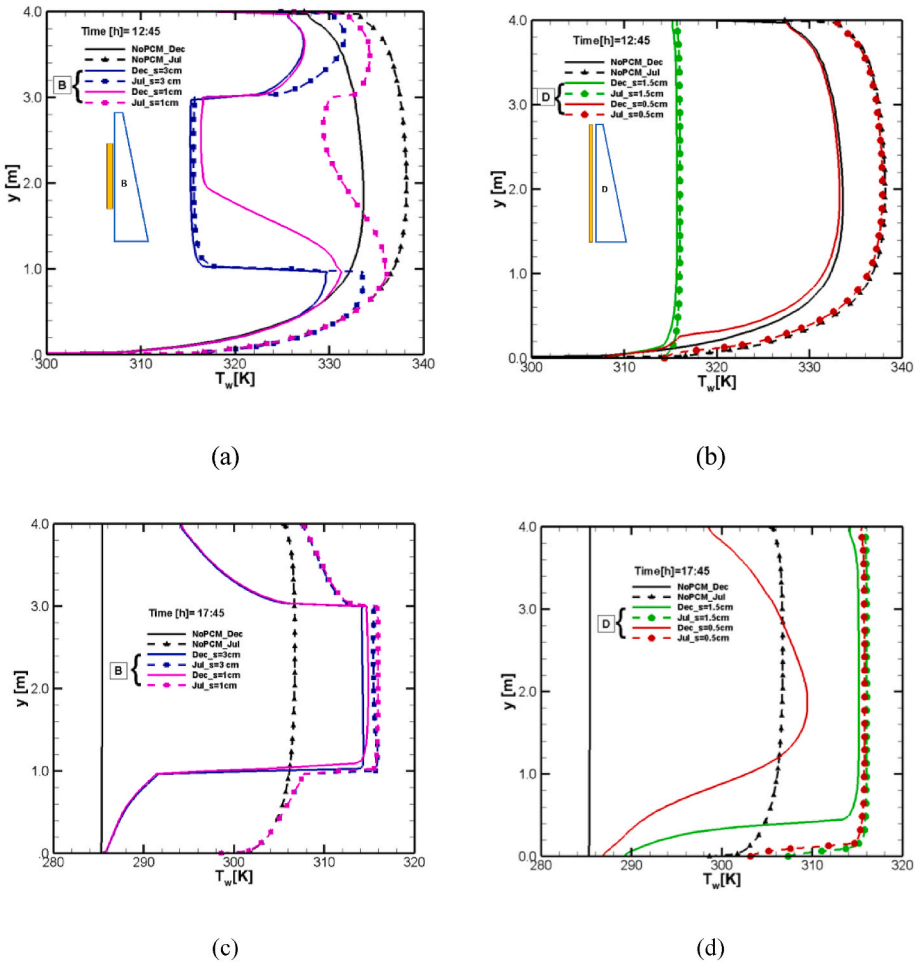


Fig. 8. Comparison of the wall temperature profiles along y for a Solar Chimney without Thermal Energy Storage (TES) and Configuration B in the range time 12:45 (a) and 17:45 (c), and Configuration D in the range time 12:45 (b) and 17:45 (d), for s = 1.0 and 3.0 in July and December.

July and December. Higher thickness is associated with the achievement of lower average temperature in both July and December. In addition, it can be seen that different configurations impact differently on the temperature of the PCM, in fact, configurations B and C (i.e., when the PCM + MF box is placed in the middle and at the top end of the chimney) have higher average temperatures but the first to reach a high temperature is configuration D, although then it is the one in which the PCM cools down first, both in summer and winter and this is mainly due to the lower thickness of the other configurations and the larger dispersive surface area.

4.3. Liquid fraction and stream functions

In Fig. 12, the liquid fraction of the PCM + MF box is shown for the different configurations (A-D) for a typical day in July and December. In the cases of s = 1.0 cm, complete melting (β = 1) is achieved for configurations B-C-D in the month of July. In December, configurations B-C with s = 1.0 cm reach β = 1, whereas configuration D doesn't reach β = 1 due to a larger dispersive surface. For s = 1.0 cm, configuration A never reaches melting because the hot air is located at the top of the channel due to convective motions, preventing the accumulation box from warming up and keeping it in constant contact with cold air. For s = 3.0 cm, the configurations A, B and C do not achieve complete melting, and the melting peak is shifted to the right due to the larger volume of the PCM. Otherwise, in configuration D, all the PCM melts during the month of July. This is why, when transitioning from s = 1.0 cm to s = 3.0 cm and tripling the volume, the accumulated energy also triples. In the other cases (A, B, C), not all the PCM volume melts. Consequently, since not all the PCM is utilized, the accumulated energy is lower.

Fig. 13 pertains to configuration D and displays the stream functions within the chimney channel, illustrating the airflow at different time intervals and how the liquid fraction of the PCM + MF box in contact with the vertical chimney wall varies. Specifically, Fig. 13a–d correspond to configuration D with an accumulation box thickness of s = 0.5 cm, while Fig. 12e–h represent the case where the accumulation box has a thickness of s = 1.5 cm. It can be observed that the liquid fraction and temperature of the PCM + MF box exhibit distinct trends based on the box thickness. For s = 0.5 cm, the box temperature peaks around 12:45, whereas for s = 1.5 cm, the temperature peak occurs later around 15:45. This behavior aligns with what was previously observed in Fig. 11a.

4.4. Mass flow rate and energy stored

Fig. 14 depicts the trend of mass flow rate in July and December for thicknesses of s = 1.0 cm and s = 3.0 cm. It can be observed that the difference becomes more pronounced as the PCM + MF box thickness increases. Consequently, with greater volume, ventilation extends over a longer period, and the decline after sunset is more gradual. Configuration A displays a more uniform pattern compared to configurations B and C because it accumulates heat at the bottom where the air is colder and then releases it. Thanks to convective motion, warm air tends to rise. Therefore, even though the accumulation is only at the base of the chimney, it is precisely there that it is most effective since the air is colder. Additionally, during winter, its downward positioning doesn't

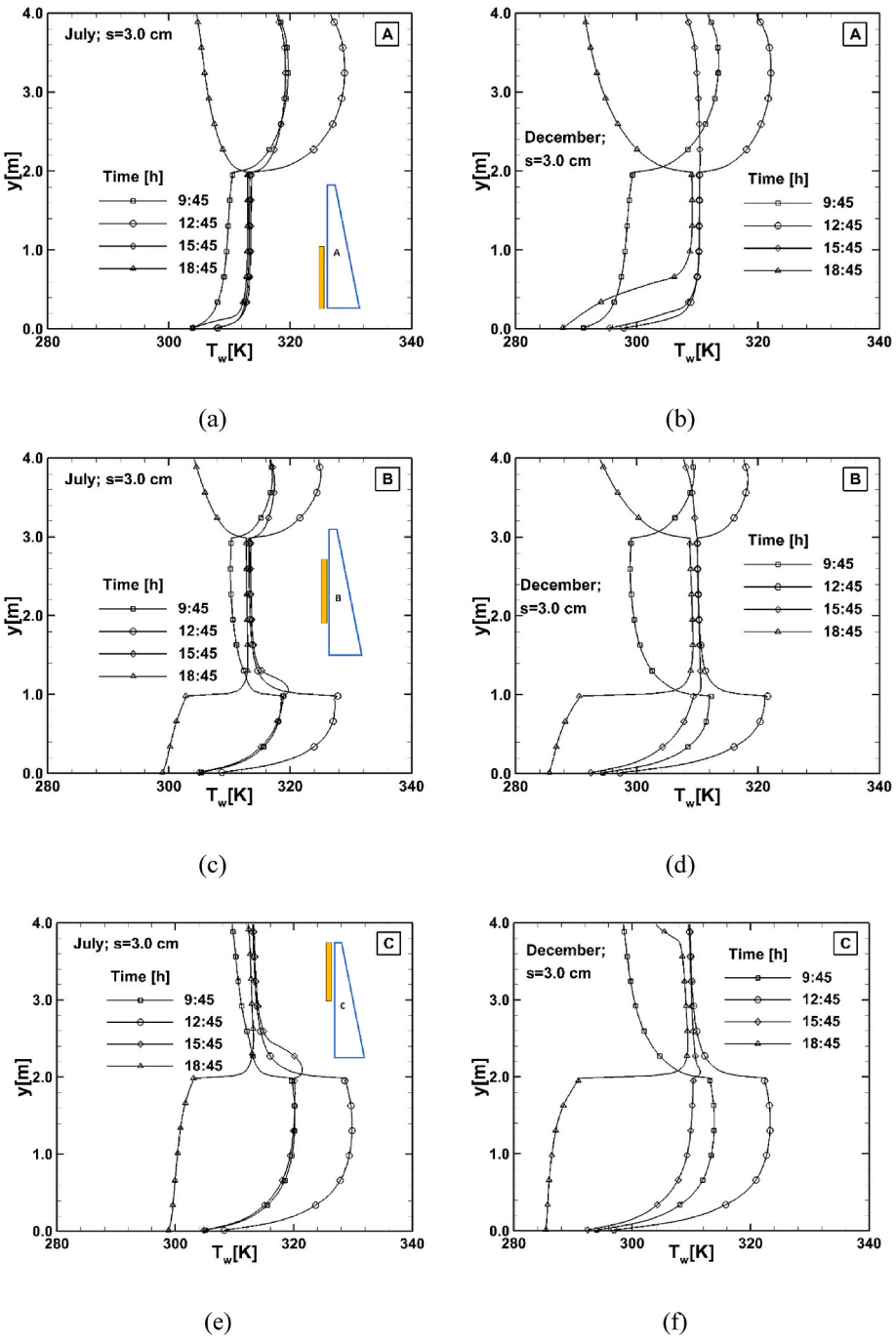


Fig. 9. Wall temperature profiles along y for s = 3.0 in the time range 9:45–18:45 in July (a, c, e) and December (b, d, f). Configuration A, B and C.

subtract heat from the upper part of the chimney. For this reason, the mass flow rate follows a more consistent pattern in configuration A.

Fig. 15 shows the accumulated energy according to different thicknesses of the PCM + MF layer and Eq. (22) was used to report the fluctuation of enthalpy for the unit of volume in the PCM.

$$\Delta h_p = \rho_p h_L \beta + \rho_p c_v (T - T_0) \tag{22}$$

where T_0 represents the ambient temperature equal to 294 K.

It can be seen that for thickness s = 1.0 cm all configurations always have the same trend. On the other hand, in Fig. 14b, configuration D has higher accumulated energy than the other three configurations, both in Winter and Summer. In configuration D, as the thickness triples, the stored energy also almost triples, whereas in the other configurations as the thickness triples, the stored energy approximately doubles (Table 6).

4.5. Velocity profiles along x-axis

Fig. 16 displays velocity profiles along the x-axis for the analyzed configurations A-D at two different times (12:45 and 15:45) and three heights of the solar chimney (y = 0.02 m, 2.00 m, and 3.98 m) during the month of July. It can be observed that at the same time, for different configurations with s = 1.0 cm at 12:45 in July, there isn't a significant difference in velocities among the various configurations, except for configuration A, which exhibits a lower velocity trend compared to the others (Fig. 16a). However, at 15:45, all configurations show similar velocities (Fig. 16b). On the other hand, when increasing the thickness from s = 1.0 cm to s = 3.0 cm, differences in velocities among the

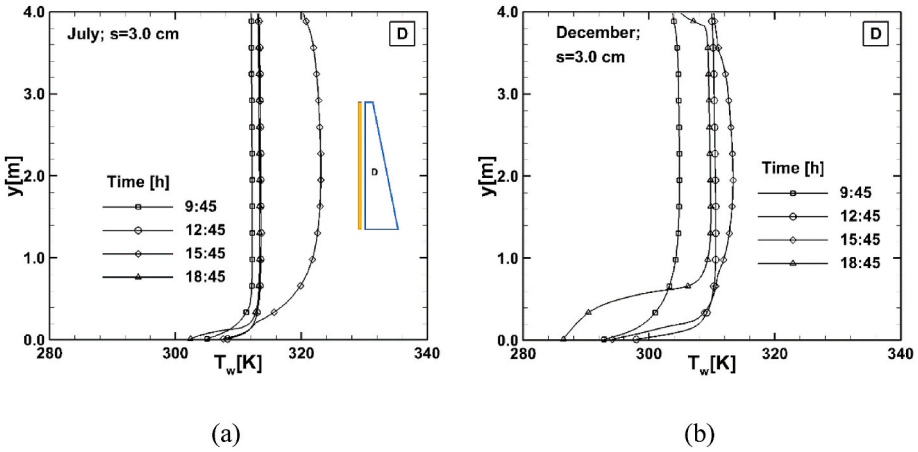


Fig. 10. Wall temperature profiles along y for s = 3.0 in the time range 9:45–18:45 in July (a) and December (b). Configuration D.

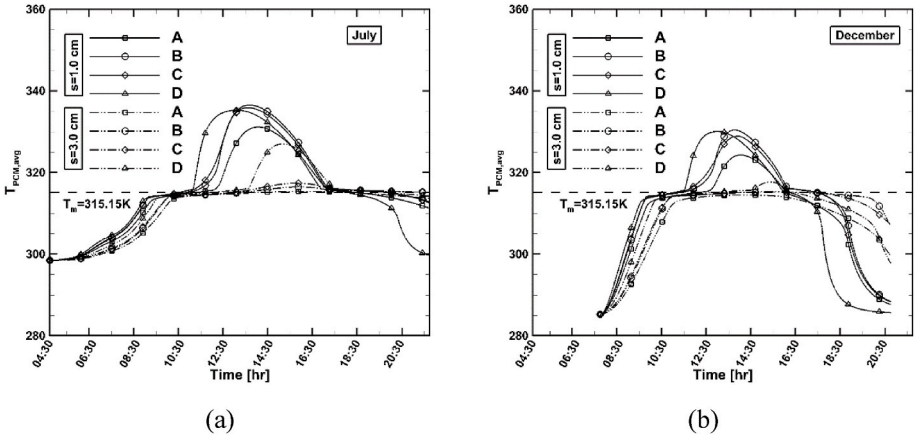


Fig. 11. Average temperature of the PCM as a function of time for s = 1.0 cm and 3.0 cm, for various configuration (A–D): (a) July and (b) December.

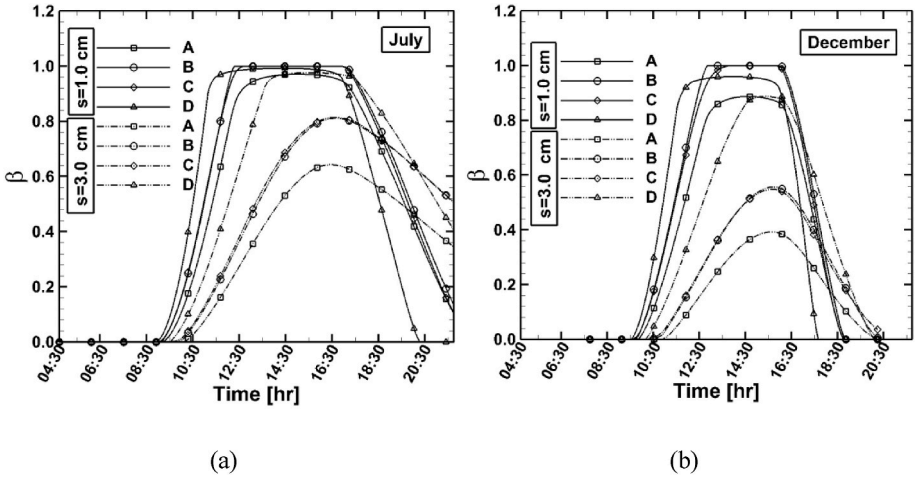


Fig. 12. Liquid fraction as a function of time in the months July and December, for various configurations (A–D): (a) July s = 1.0 cm and (b) s = 3.0 cm.

configurations become more pronounced. Notably, configuration D demonstrates a higher velocity profile compared to the others, both at 12:45 and 15:45.

Fig. 17 presents velocity profiles along the x-axis for the analyzed configurations A-D at two different times (12:45 and 15:45) and three heights of the solar chimney (y = 0.02 m, 2.00 m, and 3.98 m) during the month of December. It can be observed that at the same time, for different configurations with s = 1.0 cm in December at 12:45, there isn't a significant difference in velocities among the various configurations, except for configuration A, which displays a lower velocity trend compared to the others (Fig. 17a). However, at 15:45, similar to July, all configurations exhibit the same velocity (Fig. 17b). Increasing the thickness from s = 1.0 cm to s = 3.0 cm accentuates the velocity differences among the various configurations. Notably, configurations D

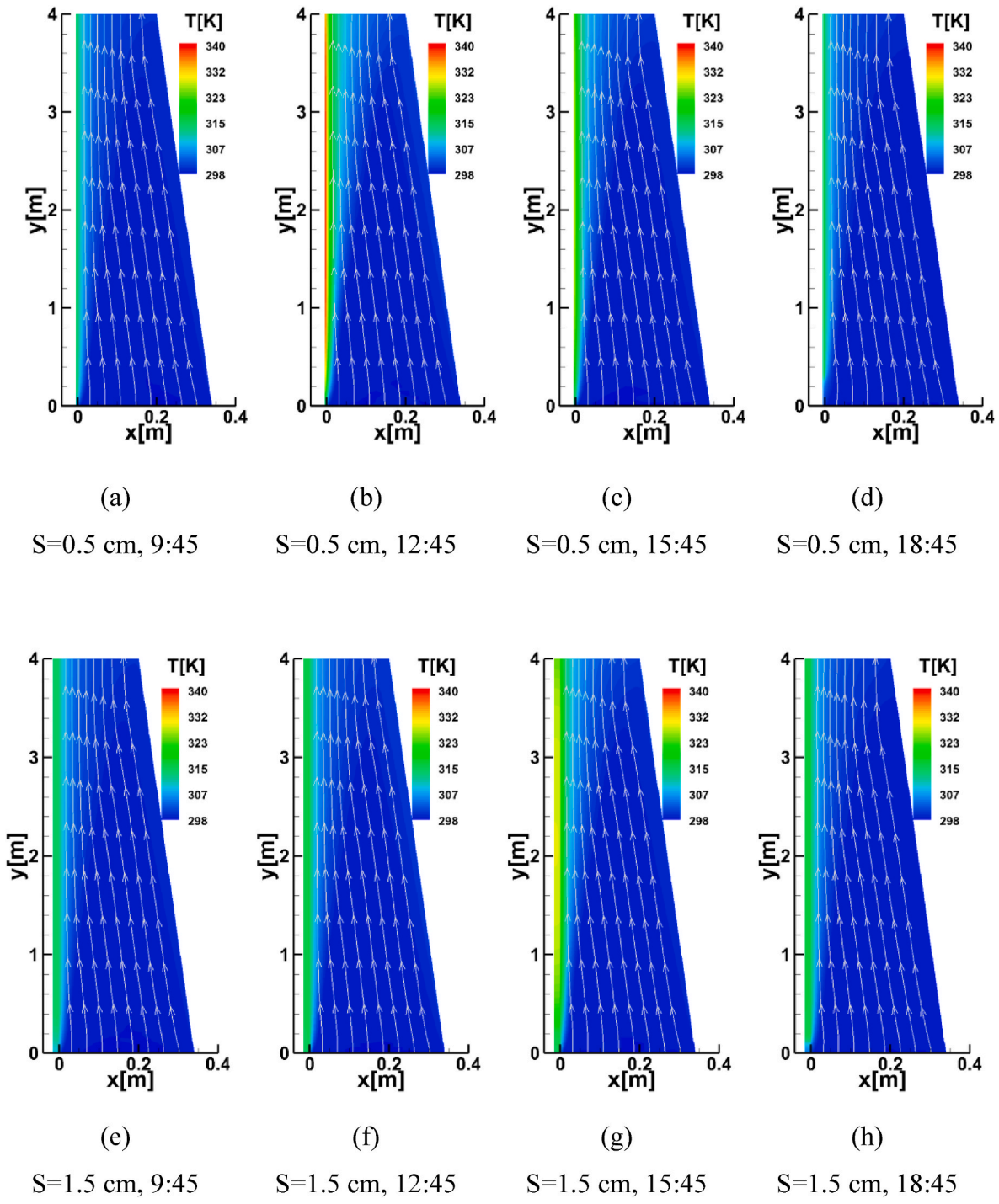


Fig. 13. Stream function with liquid fraction in the configuration D during a day of July.

and A demonstrate higher velocity profiles than the others, both at 12:45 and 15:45. A velocity peak is formed near the wall in configurations A and D, and a peak is observed toward the inclined glass in configuration A. This occurs because in configuration A, the accumulation box is located at the base of the chimney, and as one moves upward, the inclined wall gradually heats up without transferring heat to the box behind it. This observation aligns with the analysis of mass flow rate in Fig. 13.

4.6. Collector efficiency and energy density

Furthermore, the performance of the investigated solar chimney has also been evaluated to understand the efficiency of different configurations. Solar radiation on the collector (Q_s) and the heat absorbed by the collector (Q_u) have been assessed in order to calculate the efficiency of system η_{sc} [4].

$$Q_s = I \times A$$

where I is the solar radiation and A is the collector area.

$$Q_u = \dot{m}_a \times c_p \times \Delta T$$

$\dot{m}_a$ is the mass flow rate of air, c_p refers to the specific heat of air, and ΔT is the temperature difference between the outgoing air and the incoming

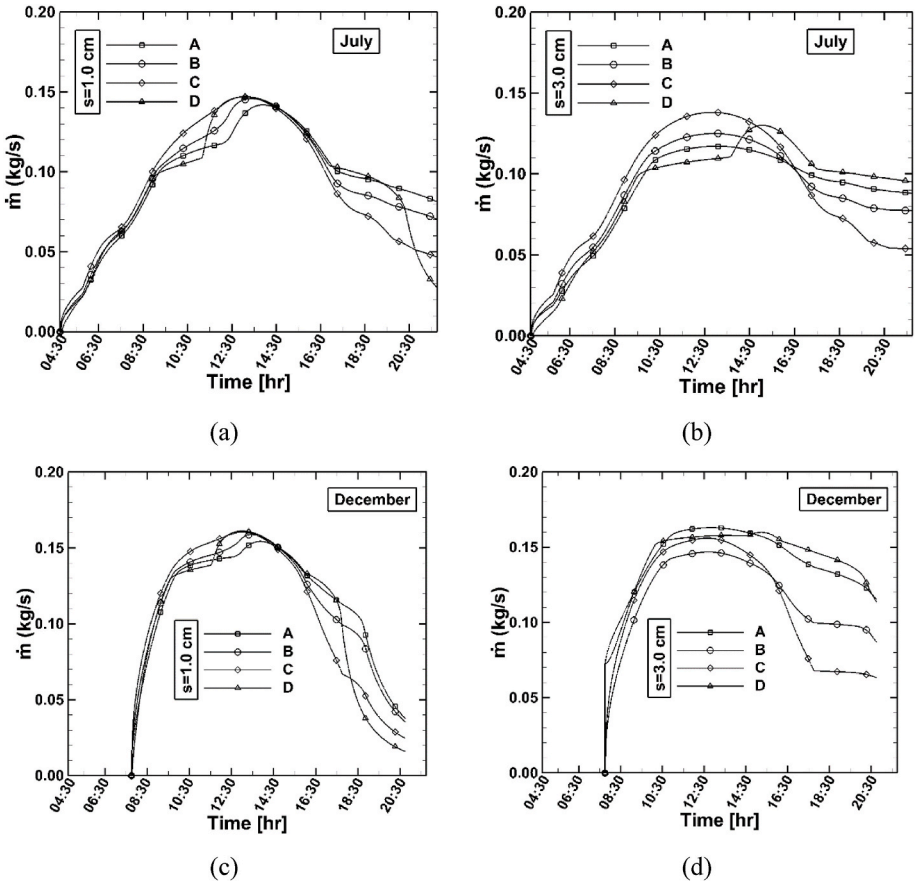


Fig. 14. Mass flow rate as a function of time in the months July and December, for various configuration (A–D): July (a) s = 1.0 cm, (b) s = 3.0 cm; December (c) s = 1.0, (d) s = 3.0 cm.

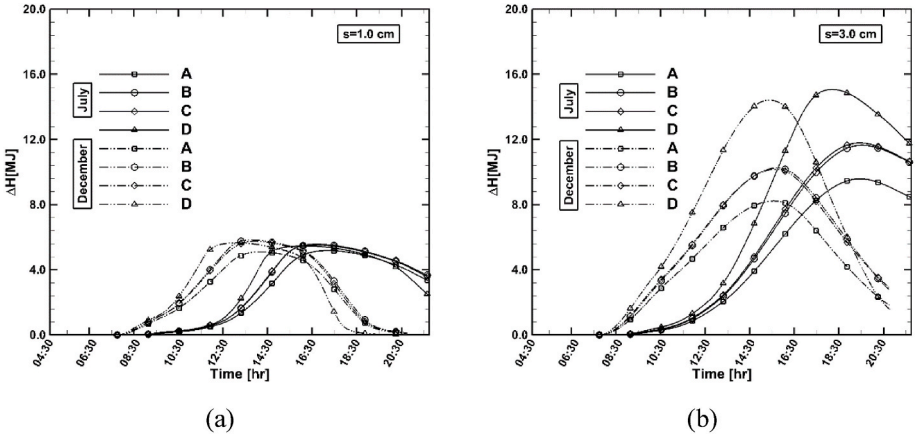


Fig. 15. Energy stored as a function of time in the months July and December, for various configuration (A–D): (a) July s = 1.0 cm and (b) s = 3.0 cm.

Table 6
Maximum value of energy stored in each configuration and percentage rise.

	Jul s = 3.0 cm	Jul s = 1.0 cm	%	Dec s = 3.0 cm	Dec s = 1.0 cm	%
A	8.1 MJ	4.92 MJ	65 %	8.23 MJ	5.1 MJ	61 %
B	9.96 MJ	5.39 MJ	85 %	10.26 MJ	5.83 MJ	76 %
C	10.12 MJ	5.36 MJ	89 %	10.18 MJ	5.76 MJ	77 %
D	14.06 MJ	5.29 MJ	166 %	14.42 MJ	5.65 MJ	155 %

air in the chimney.

The efficiency of the system is determined by

$$\eta_{sc} = \frac{Q_u}{Q_s} 100$$

From which the daily average efficiency of the chimney for various configurations has been derived and given in Table 7.

From the obtained results, it is evident that the solar chimney in configuration D with a box thickness of s = 1.50 exhibits the highest daily average efficiency, with η_{sc} = 57 % in July and η_{sc} = 51 % in December. For s = 1.0 cm, all configurations show nearly the same

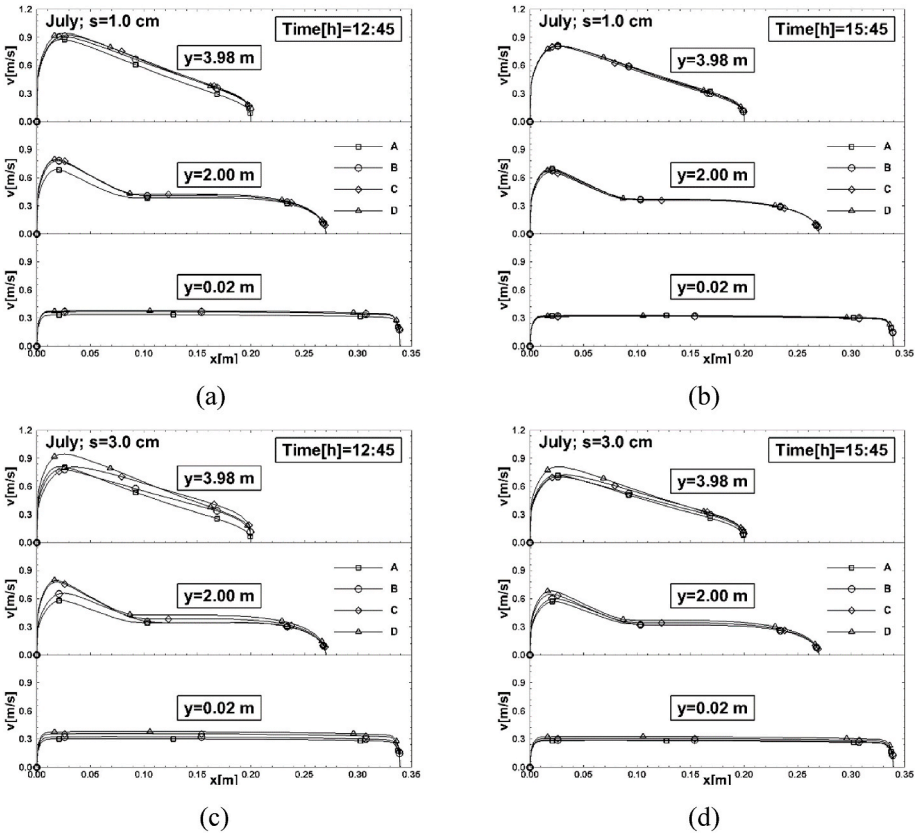


Fig. 16. Velocity profiles along x for s = 1.0 cm in July and for various configuration (A–D): (a) Time [h] = 12:45, (b) Time [h] = 15:45, and for s = 3.0 cm in July and for various configuration (A–D) (c) Time [h] = 12:45, (d) Time [h] = 15:45.

efficiency. Configuration A has a lower efficiency compared to the others in general, but it shows a velocity profile along y that is higher than that of configurations B and C, and a more consistent mass flow rate. This is because in configuration A, the PCM + MF box has a smaller impact on the functioning of the solar chimney compared to the other configurations.

Finally, the energy density has been calculated for various cases by varying the thickness of the thermal storage box. It was computed as the accumulated energy per unit volume. The energy throughout the entire day was summed and then divided by the volume of the box in the different cases. In the scenario with s = 1.0 cm, the volume is 0.02 m^3, and in the case of s = 3.0 cm, the volume is 0.06 m^3. It is worth noting that in configuration D, the box extends along the entire solar chimney wall, but the thickness is halved in order to maintain the same volume.

$$\rho_E\left[MJ/m^3\right] = \frac{\sum_{day}\Delta H}{V}$$

Both the graph, in Fig. 18, and Table 8, related to the energy density, have been presented.

The energy density is higher in the cases with a volume of 0.02 m^3, which corresponds to a thickness of s = 1.0 cm, both in the months of July and December. For cases A, B, and C, there is an approximate difference of 2×10^5 MJ when transitioning from configurations with a volume of 0.02 m^3 to those with a volume of 0.06 m^3. However, in configuration D, in December, the energy density for the s = 1.5 cm case is slightly lower than the s = 0.5 cm case. On the average day in July, there is a reversal, where the s = 1.5 cm case has a higher energy density than the s = 0.5 cm case.

The obtained results are consistent with the accumulated energy graphs (Fig. 15), as increasing the thickness of the box results in cases A, B, and C accumulating less thermal energy due to the incomplete melting of the phase change material (PCM) present in the box.

5. Conclusions

The definition of a passive system—one that collects, stores, and diffuses solar radiation heat without the use of installation—is crucial. A possible technology that can be used as a passive system is a solar chimney with latent heat storage. This study aimed to assess the effects of various storage system configurations in the solar chimney. The capacity wall is composed of a high-absorbing plate and a box with phase change material embedded in aluminium metal foam and assigned porosity values and pores per inch. Four various configurations of the box are evaluated, each with a different size and placement along the vertical wall. The findings demonstrate how the wall heats and cools both with the PCM + MF storage box, as well as how configuration, thickness, and weather affect daytime trends in liquid fraction, energy storage, and mass flow rate.

It is reported that the Configuration A, located at the base of the chimney, shows the lowest average PCM temperature and fails to achieve complete melting. It exhibits a uniform mass flow rate but the lowest overall efficiency due to its design, which restricts PCM melting. Energy accumulation increases by 65 % in July and 61 % in December when the volume tripled. Regarding Configurations B and C, positioned in the middle and at the top of the chimney, respectively, demonstrate higher average PCM temperatures and achieve complete melting. Configuration C has the highest peak mass flow rates but less uniform behavior. Both configurations show significant energy accumulation increases of 85–89 % in July and 76–77 % in December by tripling the volume. Concerning Configuration D, where the storage box spans the entire wall, maintains a more consistent wall temperature and reaches the PCM melting temperature first. It offers the highest accumulated energy increases (155 % in December and 166 % in July) and the best

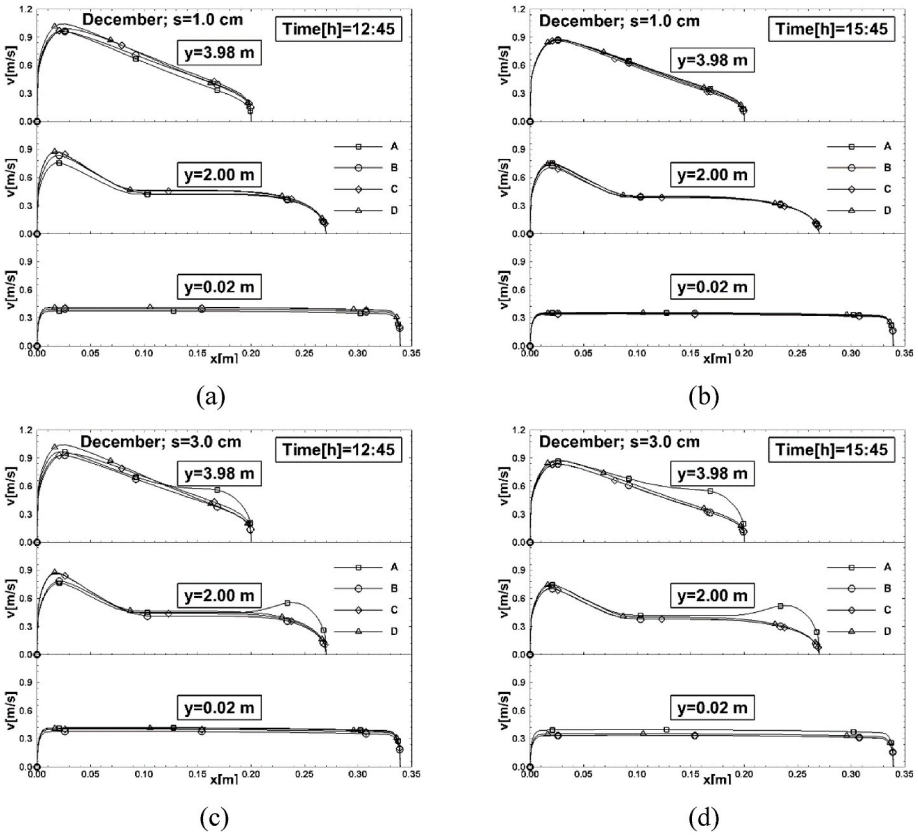


Fig. 17. Velocity profiles along x for s = 1.0 cm in December and for various configuration (A–D): (a) Time [h] = 12:45, (b) Time [h] = 15:45, and for s = 3.0 cm in December and for various configuration (A–D): (c) Time [h] = 12:45, (d) Time [h] = 15:45.

Table 7
Daily average efficiency of the chimney.

	Jul s = 3.0 cm	Jul s = 1.0 cm	Dec s = 3.0 cm	Dec s = 1.0 cm
A	32 %	23 %	28 %	19 %
B	37 %	24 %	35 %	22 %
C	37 %	24 %	35 %	22 %
D	57 %	24 %	51 %	22 %

system efficiency (57 % in July).

The work conducted has yielded a set of valuable data that elucidates the functioning of the solar chimney with a phase change material storage box. The collected data underpins future decisions to expand research on the solar chimney. In fact, potential future developments include analysing different PCM + MF configurations with varying melting temperatures more suitable for climate of Aversa (IT); exploring configurations with only PCM; comparing the resulting configurations to

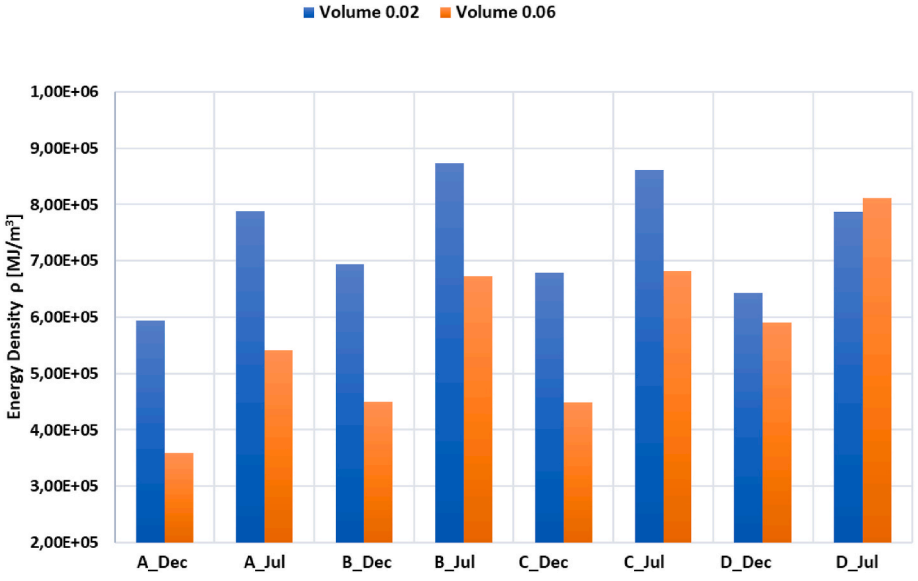


Fig. 18. Energy density for the various cases analyzed in December and July.

Table 8
Energy density.

Case	*Volume 0.02 m^3*	*Volume 0.06 m3*
A_Dec	$5{,}94 \times 10^5$	$3{,}59 \times 10^5$
A_Jul	$7{,}88 \times 10^5$	$5{,}41 \times 10^5$
B_Dec	$6{,}94 \times 10^5$	$4{,}51 \times 10^5$
B_Jul	$8{,}72 \times 10^5$	$6{,}73 \times 10^5$
C_Dec	$6{,}78 \times 10^5$	$4{,}48 \times 10^5$
C_Jul	$8{,}62 \times 10^5$	$6{,}81 \times 10^5$
D_Dec	$6{,}43 \times 10^5$	$5{,}90 \times 10^5$
D_Jul	$7{,}87 \times 10^5$	$8{,}12 \times 10^5$

the chimney without storage; and ultimately devising configurations that can be experimentally implemented.

CRediT authorship contribution statement

Sergio Nardini: Writing – review & editing, Writing – original draft, Supervision, Methodology, Conceptualization. **Bernardo Buonomo:** Writing – review & editing, Writing – original draft, Supervision, Methodology, Formal analysis, Conceptualization. **Maria Rita Golia:** Writing – original draft, Investigation, Funding acquisition, Data curation. **Oronzio Manca:** Writing – review & editing, Writing – original draft, Supervision, Formal analysis, Conceptualization.

Declaration of competing interest

The authors declare that they have no known competing financial interests or personal relationships that could have appeared to influence the work reported in this paper.

References

[1] B. Ghernaout, S. Bouabdallah, M.E.H. Attia, M. Arıcı, Z. Driss, Parametric study of the airflow structure in a solar chimney, International Journal of Heat and Technology 38 (2020) 285–292, https://doi.org/10.18280/ijht.380202.

[2] L. Cirillo, D. Ronza, V. Fardella, O. Manca, S. Nardini, Numerical and experimental investigations on a solar chimney integrated in a building facade, International Journal of Heat and Technology 33 (2015) 246–254, https://doi.org/10.18280/ijht.330433.

[3] B. Buonomo, O. Manca, S. Nardini, P. Romano, Thermal and fluid dynamic analysis of solar chimney building systems, International Journal of Heat and Technology 31 (2013) 119–126, https://doi.org/10.18280/ijht.310216.

[4] A.A.M. Omara, H.A. Mohammed, I.J. al Rikabi, M.A. Abuelnour, A.A.A. Abuelnuor, Performance improvement of solar chimneys using phase change materials: a review, Sol. Energy 228 (2021) 68–88, https://doi.org/10.1016/j.solener.2021.09.037.

[5] I. Dincer, M.A. Rosen, Thermal Energy Storage: Systems and Applications, second ed., 2011. New York.

[6] L.F. Cabeza, Advances in Thermal Energy Storage Systems: Methods and Applications, Elsevier, 2021, https://doi.org/10.1016/B978-0-12-819885-8.00030-9.

[7] H. Kotani, S.D. Sharma, Y. Kaneko, T. Yamanaka, K. Sagara, Development of solar chimney with Built-In latent heat storage material for natural ventilation. http://www.arch.eng.osaka-u.ac.jp/~labo4/www/paper-top.files/2005_pdf/05_i_01.pdf, 2005. (Accessed 20 April 2022).

[8] S.D. Sharma, H. Kotani, Y. Kaneko, T. Yamanaka, K. Sagara, Design, development of a solar chimney with Built-in latent heat storage material for natural ventilation, Int. J. Green Energy 4 (2007) 313–324, https://doi.org/10.1080/15435070701332120.

[9] Y. Kaneko, K. Sagara, T. Yamanaka, H. Kotani, Ventilation performance of solar chimney with Build-in latent heat storage. https://www.researchgate.net/publication/265989559_VENTILATION_PERFORMANCE_OF_SOLAR_CHIMNEY_WITH_BUILT-IN_LATENT_HEAT_STORAGE, 2006. (Accessed 20 April 2022).

[10] K.E. Amori, S.W. Mohammed, Experimental and numerical studies of solar chimney for natural ventilation in Iraq, Energy Build. 47 (2012) 450–457, https://doi.org/10.1016/j.enbuild.2011.12.014.

[11] N. Fadaei, A. Kasaeian, A. Akbarzadeh, S.H. Hashemabadi, Experimental investigation of solar chimney with phase change material (PCM), Renew. Energy 123 (2018) 26–35, https://doi.org/10.1016/j.renene.2018.01.122.

[12] T. Long, W. Li, Y. Lv, Y. Li, S. Liu, J. Lu, S. Huang, Y. Zhang, Benefits of integrating phase-change material with solar chimney and earth-to-air heat exchanger system for passive ventilation and cooling in summer, J. Energy Storage 48 (2022) 104037, https://doi.org/10.1016/j.est.2022.104037.

[13] Y. Cao, N. Sinaga, S. Pourhedayat, H.S. Dizaji, Innovative integration of solar chimney ventilator, solar panel and phase change material; under real transient weather condition of Hong Kong through different months, Renew. Energy 174 (2021) 865–878, https://doi.org/10.1016/j.renene.2021.04.146.

[14] S. Nateghi, M.H. Jahangir, Performance evaluation of solar chimneys in providing the thermal comfort range of the building using phase change materials, Cleaner Materials 5 (2022) 100120, https://doi.org/10.1016/j.clema.2022.100120.

[15] R. Tariq, C.E. Torres-Aguilar, N.A. Sheikh, T. Ahmad, J. Xamán, A. Bassam, Data engineering for digital twining and optimization of naturally ventilated solar façade with phase changing material under global projection scenarios, Renew. Energy 187 (2022) 1184–1203, https://doi.org/10.1016/j.renene.2022.01.044.

[16] Y. Li, S. Liu, Numerical study on thermal behaviors of a solar chimney incorporated with PCM, Energy Build. 80 (2014) 406–414, https://doi.org/10.1016/j.enbuild.2014.05.043.

[17] S. Liu, Y. Li, An experimental study on the thermal performance of a solar chimney without and with PCM, Renew. Energy 81 (2015) 338–346, https://doi.org/10.1016/j.renene.2015.03.054.

[18] Y. Li, S. Liu, J. Lu, Effects of various parameters of a PCM on thermal performance of a solar chimney, Appl. Therm. Eng. 127 (2017) 1119–1131, https://doi.org/10.1016/j.applthermaleng.2017.08.087.

[19] M.E. Tiji, M. Eisapour, R. Yousefzadeh, M. Azadian, P. Talebizadehsardari, A numerical study of a PCM-Based passive solar chimney with a finned absorber, J. Build. Eng. 32 (2020) 101516, https://doi.org/10.1016/j.jobe.2020.101516.

[20] J. Xamán, R. Vargas-López, M. Gijón-Rivera, I. Zavala-Guillén, M.J. Jiménez, J. Arce, Transient thermal analysis of a solar chimney for buildings with three different types of absorbing materials: copper plate/PCM/concrete wall, Renew. Energy 136 (2019) 139–158, https://doi.org/10.1016/j.renene.2018.12.106.

[21] B. Buonomo, H. Celik, D. Ercole, O. Manca, M. Mobedi, Numerical study on latent thermal energy storage systems with aluminum foam in local thermal equilibrium, Appl. Therm. Eng. 159 (2019) 113980, https://doi.org/10.1016/j.applthermaleng.2019.113980.

[22] M. Ashouri, A. Hakkaki-Fard, Improving the performance of the finned absorber inclined rooftop solar chimney combined with composite PCM and PV module, Sol. Energy 228 (2021) 562–574, https://doi.org/10.1016/j.solener.2021.09.088.

[23] S. Huang, W. Li, J. Lu, Y. Li, Z. Wang, S. Zhu, Experimental study on thermal performances of a solar chimney with and without PCM under different system inclination angles, Energy (Calg.) 290 (2024) 130154, https://doi.org/10.1016/j.energy.2023.130154.

[24] B. Buonomo, L. Capasso, A. Diana, O. Manca, S. Nardini, A numerical analysis on a solar chimney with an integrated latent heat thermal energy storage, AIP Conf. Proc. 2191 (2019) 020029, https://doi.org/10.1063/1.5138762.

[25] B. Buonomo, L. Capasso, O. Manca, F. Menale, S. Nardini, A numerical analysis on a solar chimney with an integrated thermal energy storage with phase change material in metal foam, E3S Web of Conferences 197 (2020) 08001, https://doi.org/10.1051/e3sconf/202019708001.

[26] B. Buonomo, M.R. Golia, O. Manca, S. Nardini, A numerical study on an integrated solar chimney with latent heat thermal energy storage in various arrangements, Int. J. Sustain. Dev. Plann. 17 (2022) 1693–1698, https://doi.org/10.18280/ijsdp.170601.

[27] A. Pasupathy, L. Athanasius, R. Velraj, R.V. Seeniraj, Experimental investigation and numerical simulation analysis on the thermal performance of a building roof incorporating phase change material (PCM) for thermal management, Appl. Therm. Eng. 28 (2008) 556–565, https://doi.org/10.1016/j.applthermaleng.2007.04.016.

[28] M.A.R. Sharif, A. Banerjee, Numerical analysis of heat transfer due to confined slot-jet impingement on a moving plate, Appl. Therm. Eng. 29 (2009) 532–540, https://doi.org/10.1016/j.applthermaleng.2008.03.011.

[29] M.A. Bashir, H.M. Ali, Numerical assessment of the effect of tube geometries on the performance of phase change material (PCM) integrated solar receiver for dish-micro gas turbine systems, J. Energy Storage 68 (2023) 107725, https://doi.org/10.1016/j.est.2023.107725.

[30] B.E. Launder, D.B. Spalding, The numerical computation of turbulent flows, Comput. Methods Appl. Mech. Eng. 3 (1974) 269–289, https://doi.org/10.1016/0045-7825(74)90029-2.

[31] A. Ayadi, Z. Driss, A. Bouabidi, M.S. Abid, Experimental and numerical study of the impact of the collector roof inclination on the performance of a solar chimney power plant, Energy Build. 139 (2017) 263–276, https://doi.org/10.1016/j.enbuild.2017.01.047.

[32] A. Bhattacharya, V.V. Calmidi, R.L. Mahajan, Thermophysical properties of high porosity metal foams, Int J Heat Mass Transf 45 (2002) 1017–1031, https://doi.org/10.1016/S0017-9310(01)00220-4.

[33] A. Ayadi, A. Bouabidi, Z. Driss, M.S. Abid, Experimental and numerical analysis of the collector roof height effect on the solar chimney performance, Renew. Energy 115 (2018) 649–662, https://doi.org/10.1016/j.renene.2017.08.099.

[34] V.R. Voller, C. Prakash, A fixed grid numerical modelling methodology for convection-diffusion mushy region phase-change problems, Int J Heat Mass Transf 30 (1987) 1709–1719, https://doi.org/10.1016/0017-9310(87)90317-6.

[35] J. Yang, X. Du, L. Yang, Y. Yang, Numerical analysis on the thermal behavior of high temperature latent heat thermal energy storage system, Sol. Energy 98 (2013) 543–552, https://doi.org/10.1016/j.solener.2013.10.028.

[36] Inc., Canonsburg. ANSYS, ANSYS, ANSYS Fluent Theory Guide, 2020, 2020.

[37] C. Gau, R. Viskanta, Melting and solidification of a pure metal on a vertical wall, J Heat Transfer 108 (1986) 174–181, https://doi.org/10.1115/1.3246884.

[38] M. Miyamoto, Y. Katoh, J. Kurima, H. Sasaki, Turbulent free convection heat transfer from vertical parallel plates, in: Proceeding of International Heat Transfer Conference 8, 1986, pp. 1593–1598, https://doi.org/10.1615/IHTC8.3200. Begellhouse, Connecticut.